

Full length article

The interplay and impact of strain and defect association on the conductivity of rare-earth substituted ceria

George F. Harrington^{a, b, d, c, *}, Lixin Sun^e, Bilge Yildiz^{e, d}, Kazunari Sasaki^{a, b, c},
Nicola H. Perry^{c, f}, Harry L. Tuller^{d, c}

^a Center of Coevolutionary Research for Sustainable Communities (C²RSC), Kyushu University, 744 Motoooka, Nishi-ku, Fukuoka, 819-0395, Japan

^b Next-Generation Fuel Cell Research Centre, Kyushu University, 744 Motoooka, Nishi-ku, Fukuoka, 819-0395, Japan

^c International Institute for Carbon-Neutral Energy Research (WPI-I²CNER), Kyushu University, 744 Motoooka, Nishi-ku, Fukuoka, 819-0395, Japan

^d Department of Materials Science and Engineering, Massachusetts Institute of Technology, 77 Massachusetts Ave., Cambridge, MA, 02139, USA

^e Department of Nuclear Science and Engineering, Massachusetts Institute of Technology, 77 Massachusetts Ave., Cambridge, MA, 02139, USA

^f Department of Materials Science and Engineering and Materials Research Laboratory, University of Illinois at Urbana-Champaign, Urbana, IL, 61801, USA

ARTICLE INFO

Article history:

Received 13 September 2018

Received in revised form

14 December 2018

Accepted 31 December 2018

Available online 3 January 2019

Keywords:

Ionic diffusion

Point defects

Lattice strain

Thin films

Ceria

ABSTRACT

The effects of strain on the ionic conductivity of rare-earth substituted CeO₂ have been extensively studied, but the results have been inconsistent and focused upon the 'optimised' conductors such as Gd or Sm substituted CeO₂ where defect association is minimised. By thermally annealing epitaxial films deposited by pulsed laser deposition, we varied the strain systematically, whilst avoiding any influence from interfacial or grain boundary effects. The activation energy of the in-plane conductivity was found to increase with increasing compressive biaxial strain, which was quantitatively in excellent agreement with previous computational and experimental studies. These results provide a much needed quantitative consensus on the effects of lattice strain on ionic transport. Furthermore, we demonstrate that the change in the activation energy for Yb-substituted CeO₂ is around three times that for Gd or La substitutions for the same applied strain, indicating the important role played by defect association. These results have significant implications for ionic transport at reduced or ambient temperatures, where changes in conductivity due to strain may be several orders of magnitude larger for 'non-optimised' conductors compared with 'optimised' conductors. We rationalise our results by considering the defect-defect interactions in these materials and through force-field calculations.

© 2019 Acta Materialia Inc. Published by Elsevier Ltd. All rights reserved.

1. Introduction

Ionic conducting materials form the foundation of a wide range of electrochemical devices. Examples include Li⁺ or Na⁺ conductors for batteries, as well as O²⁻ and OH⁻ conductors for fuel cells, electrolyzers and gas separation membranes. Typically, a substituting aliovalent species generates compensating ionic defects that facilitate ionic transport, but unlike semiconductors, ionic conductors show a maximum followed by a decrease in the conductivity as the concentration of the substituent species is increased. This is caused by defect-defect interactions, or defect

association, whereby the mobile species can be bound to the substituting defect, limiting the ionic conductivity [1–4]. In order to design better ionic conductors for future electrochemical devices, a better physical understanding of defect association is imperative.

Defect-defect interactions have probably been studied in the most detail for the fluorite-structured materials, CeO₂ and ZrO₂, which despite decades of searching for superior alternatives, remain the most technologically relevant solid oxygen ion conductors. Oxygen vacancies are incorporated into the material by substitution of lower valent cations, creating a solid solution with, for example, a rare-earth oxide.



Conductivity occurs via an oxygen vacancy hopping mechanism and can be expressed as

* Corresponding author. Center of Coevolutionary Research for Sustainable Communities (C²RSC), Kyushu University, 744 Motoooka, Nishi-ku, Fukuoka, 819-0395, Japan.

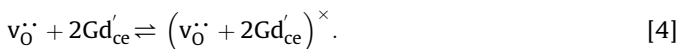
E-mail address: harrington.frederick.george.302@m.kyushu-u.ac.jp (G.F. Harrington).

$$\sigma = [v_{\text{O}}^{\bullet}] \{1 - [v_{\text{O}}^{\bullet}]\} N \frac{\sigma_0}{T} \exp\left(-\frac{E_a}{kT}\right), \quad [2]$$

where $[v_{\text{O}}^{\bullet}]$ is the site fraction of oxygen vacancies, N is the anion site concentration per unit volume, E_a is the activation energy, and σ_0 contains the oxygen vacancies' charge, the jump distance, the jump attempt frequency, geometric and entropic terms [4].

One might expect the conductivity to increase continuously as more substituted cations are introduced, but instead a maximum conductivity is observed at a concentration of around 10 mol.% in Gd-substituted CeO_2 . The reason for this effect is that interactions between the introduced defects modify the energy barriers for hopping between anion sites and destroy the degeneracy of the sites.

In simple terms, defects can be thought of as partially compensated dimers or neutral trimers, such as



More complex defect structures may also form in real systems [5–7]. Defect-defect interactions are ultimately the cause of the limit in the total conductivity [3,8,9]. Moreover, the transport properties are sensitive to the size of the substituted cation, such that the activation energy increases for cations both smaller and larger than Gd [10]. Atomistic calculations have shown that the defect association in CeO_2 is both a function of the elastic and electrostatic interactions between the defects [11,12]. Therefore the current state-of-the-art ionic conductors are 'optimised' both in terms of the size and concentration of the substituted cations to balance the effects of charge carrier concentration and defect association.

Because of this apparent limit to the conductivity, attention has turned to other methods to increase the conductivity of ionic conductors beyond what one can achieve by optimising the composition. One such method is lattice strain, whereby a mechanical strain is applied, deforming the lattice. A large number of computational simulations have addressed this topic for CeO_2 and ZrO_2 , and are in reasonable agreement [13–26]. All predict a lowering of the migration barrier with tensile strain, and an increase in the migration barrier for compressive strain.

Experimentally the effect of strain has been primarily studied in the form of thin films and multilayers [23,27–44], and has been summarised in recent reviews [45–47]. Unfortunately, despite a substantial number of experimental works investigating these effects, the vast majority of the results are inconsistent with both each other and the computational work, and in some cases, highly controversial.

Several reasons might be postulated as to why the range of experimental work is in such poor agreement. The first is the challenge in measuring the resultant conductivity while applying strains to oxide materials. Typically, this is done at a hetero-interface, with a specifically chosen lattice mismatch, which results in a localised strained region in the vicinity of the interface, provided a coherent interface is formed. But this interfacial strain is difficult to control due to the formation of dislocations and grain boundaries, and also non-trivial to characterise because of the small volumes involved. By decreasing film thickness, the volume fraction of the strained region is increased and changes in conductivity can be attributed to lattice strain. However, measuring oxygen ion conductivity in such exceptionally thin films can lead to erroneous results due to electrical leakage through the substrate

[30] or sample testing setup [48], as well as the influence of adsorbed protons [49].

Perhaps the most significant challenge faced when measuring the effects of strain on conductivity is the presence of grain boundaries in thin films and multilayers. For physical vapour grown films, small columnar grains, oriented along the growth direction, often form, resulting in a high density of grain boundaries perpendicular to the surface/interface. Grain boundaries can act to relieve interfacial strains, and are often heterogeneously distributed over the thickness of the layers [32,50]. Furthermore, grain boundaries are often blocking, and can influence the total conductivity and activation energy as a function of grain size and texture [51,52]. It is highly non-trivial to separate out the grain and grain boundary contributions in thin films [53] and therefore thickness dependent studies of thin films, where a change in the transport properties is observed, must be treated with caution [32].

Direct comparisons between reported results are further complicated due to the differences in the ways they are characterised. Due to the challenging nature of the experiments required, often, the strain state of the films is not assessed both out-of-plane and in-plane, the microstructure not evaluated in detail, or checks made to ensure that the conductivity is ionic in the films. Furthermore, the strain state (uniaxial, biaxial, hydrostatic), and the relative direction in which the conductivity is measured is often not consistent across the literature, although this relationship is predicted to lead to differences in observed changes [14,54]. Together this makes a quantitative comparison between different experimental and computational studies of limited use.

Much of the work so far on the effects of strain on transport properties has focused on the so-called 'optimised' ionic conductors, such as *commercial* electrolytes Y-stabilised ZrO_2 or Gd- or Sm-substituted CeO_2 . Very little attention has been paid to 'non-optimised' electrolytes where defect-defect interactions are much more significant. However, as the defect association limits the conductivity for these materials, a much larger enhancement in transport properties (or a less significant reduction) due to strain may be possible. In fact, classical force field studies looking at rare-earth substituted CeO_2 , have shown that the rare-earth cation leading to the lowest migration barrier switches from Nd at 0% strain to Sm at >4% strain [21].

In this report, we show that through careful experimental design we can build a quantitative consensus between experimental and computational studies of the effects of lattice strain on ionic conduction in rare-earth substituted CeO_2 . By growing relatively thick (100 nm) epitaxial films and subjecting them to post-annealing at different temperatures, we show that lattice strain occurring during growth can be subsequently modified, while avoiding complications due to grain boundaries. We demonstrate that in-plane compressive strain leads to an increase in the activation energy of the in-plane conductivity, which is consistent with other experimental and computational work.

In addition to the 'optimised' conductors, we also examine the effect of strain on the so-called 'non-optimised' conductors, where defect association is more significant. The substituents used include La, Gd, and Yb, which represent an ionic radii mismatch with the host Ce lattice of 19.6%, 8.6%, and 1.5% respectively. Here Gd substituted CeO_2 is the state-of-the-art electrolyte and represents the 'optimised' conductor, whereas La and Yb substituted CeO_2 are 'non-optimised'. We show that much larger modifications in conductivity may be achieved in Yb-substituted CeO_2 due to stronger defect-defect interactions. This also demonstrates the potential of studying the strain dependence of activation barriers as a means for examining defect association in ionically conducting materials.

2. Experimental

2.1. Target synthesis

Ceramic targets for pulsed laser deposition (PLD) of 5 at.% rare-earth substituted CeO_2 , ($\text{RE}_{0.05}\text{Ce}_{0.95}\text{O}_{2-\delta}$; RE:CeO₂, RE = La, Gd, Yb), were synthesised from nitrate precursors ($\text{Ce}(\text{NO}_3)_3 \cdot 6\text{H}_2\text{O}$, $\text{Gd}(\text{NO}_3)_3 \cdot 6\text{H}_2\text{O}$ (≥ 99.9 , Sigma Aldrich Co., USA), $\text{La}(\text{NO}_3)_3 \cdot 6\text{H}_2\text{O}$, $\text{Yb}(\text{NO}_3)_3 \cdot n\text{H}_2\text{O}$ (≥ 99.9 , Wako Pure Chemical Industries, Ltd., Japan)). The precursors were dissolved in deionized water and heated on a hot plate set to 150 °C while stirred until the water had evaporated, then subsequently calcined at 900 °C. The powders were then ground, uniaxially pressed at ~25 MPa into cylindrical pellets and sintered at 1500 °C for 10 h. Smaller pellets were also pressed and sintered for conductivity measurements on bulk samples. BaZrO_3 (BZO, 98%, Sigma Aldrich Co., USA) and SrTiO_3 (STO, 99.9%, Wako Pure Chemical Industries, Ltd., Japan) powders were uniaxially pressed in the same way and sintered for 10 h at 1650 °C and 1500 °C respectively. Phase purity was confirmed for all samples using X-ray diffraction.

2.2. Thin film fabrication

Films were deposited on 10 × 10 mm (001) MgO substrates (CrysTec GmbH, Germany) by PLD (AOV Co Ltd., Japan) using a 248 nm KrF excimer laser (Lambda Physik COMPex 102) operating at 2 Hz. The laser energy was set to 250 mJ, measured directly outside the chamber as 155 mJ, and focused to an area of about 5 mm² yielding a fluence of approximately 3.1 J cm⁻². The substrates were heated to 600 °C (according to the manufacturer's calibration) from behind using an IR lamp. Prior to deposition, ~200 nm thick Pt films were deposited on the backside of the MgO substrates at room temperature by DC sputtering (TS-DC.RF303, Pascal Corp., Japan) to facilitate effective heating of the substrate from the IR lamp. The oxygen pressure during deposition was kept at 2.5 Pa, and the target and substrate were continuously rotated. For each sample, 5 nm of BZO was deposited followed by 5 nm of STO then 100 nm of RE:CeO₂. For each material the growth rates were calibrated using x-ray reflectivity. After deposition the samples were cooled at the deposition pressure for over 1 h. The deposition conditions remained identical for all samples in this study. After growth the films were annealed at different temperatures to relax the strain occurring during growth. The films were annealed in air in a box furnace at either 600 °C, 800 °C, or 1000 °C for 6 h with a 5° min⁻¹ heating/cooling rate.

2.3. Structural characterisation

The orientation, crystalline quality and lattice parameters were evaluated using X-ray diffraction on a diffractometer with a five axis goniometer, and Cu rotating anode generator (XRD, Smartlab, Rigaku Corp. Japan). For the out-of-plane symmetrical $2\theta/\omega$ scans and the asymmetrical reciprocal space maps (RSMs) a 2-bounce Ge (022) monochromator was used. For the in-plane lattice parameter measurements, the sample was placed in a grazing incidence and exit geometry and the detector position scanned in the $2\theta_\chi$ axis, which moves perpendicularly to the conventional 2θ axis.

Oxygen-cation bond lengths in the films were investigated using Raman spectroscopy (inVia Raman Microscope, Renishaw, UK) using a 532 nm light source. Peaks were fitted using a Lorentzian function, yielding an error on the peak position <0.15 cm⁻¹.

Cross sections of the films were prepared for transmission electron microscopy (TEM) using a 'lift-out' technique on a dual-beam focused ion beam/scanning electron microscope (FIB/SEM, Nanolab 600i, FEI Company, USA). Sections were taken out of an

area underneath an electrode approximately in the centre of the films after electrical measurements had been performed. The area was prepared and thinned at 30 kV, then further thinning carried out at 5 kV and then 2 kV to reduce amorphous damage to the lamellae. The microstructure, orientation and crystalline quality of the films was analysed using a double aberration-corrected (Cs-corrector on the imaging lens and probe forming lens) TEM (JEM-ARM200F, JEOL Ltd, Japan) operating at 200 kV.

2.4. Electrical characterisation

To measure the conductivity of the films, ~200 nm thick Pt interdigitated electrodes were deposited on the surface using DC sputtering (TS-DC.RF303, Pascal Corp, Japan). The electrode geometry was defined using a shadow mask with an electrode width of 220 μm and spacing of 180 μm as measured by an optical microscope. Ag wires were attached to the electrodes using Ag paint and annealed at 250 °C to ensure good electrical and mechanical contact. For the pellets, Ag paint was painted over two surfaces to create a well-defined area and to contact the Ag wires.

The samples were then positioned in a furnace using a custom made sample holder, where the wires were shielded using alumina tubes coated in Pt paint. During measurements the temperature was accurately determined using a thermocouple set directly next to the sample, and the pO₂ kept to 0.21 atm using a flowing O₂/N₂ mix. Measurements were taken as a function of temperature from 80 °C to 520 °C, both up and down in temperature to ensure reversibility, with the furnace being allowed to equilibrate for 1 h between each electrical measurement.

In-plane conductivity was determined from 2-point impedance measurements (Alpha-A Frequency Analyser, Novocontrol Technologies GmbH & Co. KG, Germany). For all samples, an amplitude of 0.5 V and a frequency range of 1 MHz to 0.1 Hz, with zero DC bias was utilized. The impedance spectra were fitted with Z-View software. Examples of the impedance spectra are shown in the form of Nyquist plots for the films and pellets in Figs. S3 and S4, respectively, in the Supplementary Information.

2.5. Classical force field simulations

Simulations were performed with the LAMMPS package [55]. Rigid ion potentials with short range interactions and long range coulombic interactions were employed to describe the inter-atomic interactions in ceria [56], and are listed in Table S2 in the Supplementary Information. This set of potentials can capture the lattice parameter for substituted ceria and the non-linear dependence of oxygen diffusivity on substituent concentration.

A 6 × 6 × 6 supercell with 2592 atoms was used. The single oxygen vacancy migration barrier was computed by moving a single vacancy to its nearest neighbour site with the nudged elastic band method. We computed the migration barrier at different concentration and defect configurations. For dilute defect concentration, only one oxygen vacancy and two substituent cations are introduced in the simulation, equivalent to 0.2 at.%. For higher defect concentrations, the substituent cations, RE³⁺ are randomly distributed in the supercell, replacing a host cation Ce⁴⁺. The charge-compensating oxygen vacancies are initially introduced randomly but their positions are relaxed to equilibrium by running molecular dynamics at 1273 K for 100 ps and quenching back to 0 K.

At high defect concentration, the migration barrier greatly depends on the initial and final configuration. Thus, we computed >100 possible migration paths for 5 at.% and 10 at.% substituted ceria. For each migration path, one oxygen vacancy migrates from its initial position through a saddle point at a cation-cation edge to a final position. The overall potential energy for the initial and final

configuration are labelled as E_{ini} and E_{final} . The migration barrier ranges from 0 to 1.6 eV as shown in [Supplementary Fig. S5](#). But once the migration barriers are categorized by the type of cation-cation edge at the saddle point, they follow the Brønsted-Evans-Polanyi (BEP) relationship $E_{\text{mig}} = \alpha(E_{\text{fin}} - E_{\text{ini}}) + E_{\text{b}}^0$. The effective migration barrier E_{b}^0 can then be fitted to characterise the “pure” migration barrier, since all defect association components are extracted by removing the $\alpha(E_{\text{fin}} - E_{\text{ini}})$ term.

3. Results and discussion

[Fig. 1b](#) shows the XRD $2\theta/\omega$ scans of the RE:CeO₂ films (RE = La, Gd, and Yb), after annealing for 6 h at different temperatures to relax the lattice strain occurring during deposition. The 100 nm thick RE:CeO₂ layers can be seen to have a single out-of-plane (001) orientation, and the (002) reflections of the 5 nm thick BZO and STO buffer layers appear as broad overlapping peaks at around 43–47°. From the XRD data the orientation relationships for the films could be identified as

RE:CeO₂ (001)||STO(001)||BZO(001)||MgO(001)

RE:CeO₂ [110]||STO[100]||BZO[100]||MgO[100]

The rocking curves of the RE:CeO₂ (002) reflections had a full

width half maximum of $<1^\circ$ indicating good crystalline growth with a low mosaic spread (shown in [Fig. S1](#) in the Supplementary Information).

[Fig. 1c](#) shows in detail the RE:CeO₂ (002) peaks from the $2\theta/\omega$ scans. A clear shift in peak position to higher angles can be seen for higher temperature heat treatments, indicating a shrinking of the out-of-plane lattice parameter for higher temperatures. The opposite trend is seen for the RE:CeO₂ (220) peaks in the $2\theta_\chi/\phi$ scans ([Fig. S2](#) in the Supplementary Information) signifying an expansion of the in-plane lattice parameters. These changes are also apparent in the RSMs shown in [Fig. 1d](#) and [e](#), showing a shift in the position of the RE:CeO₂ (204) maxima towards the lattice parameter of the bulk material with higher temperature heat treatments.

Raman spectroscopy is a complementary technique to XRD and can be used to directly probe bond lengths in a material. For the films in this study, a single peak was observed in the Raman spectra that was assigned to the oxygen-cation stretching mode with F_{2g} symmetry [57], as shown in [Fig. 1f](#). As with the XRD peak positions, a shift in the Raman F_{2g} peaks is also seen for different heat treatments. As the temperature of the heat treatment is increased, the F_{2g} peaks display a blueshift to higher wavenumbers, corresponding to a reduction in bond length.

The lattice parameters extracted from peak positions in the out-of-plane $2\theta/\omega$ scans and in-plane $2\theta_\chi/\phi$ scans are plotted in [Fig. 2a](#)

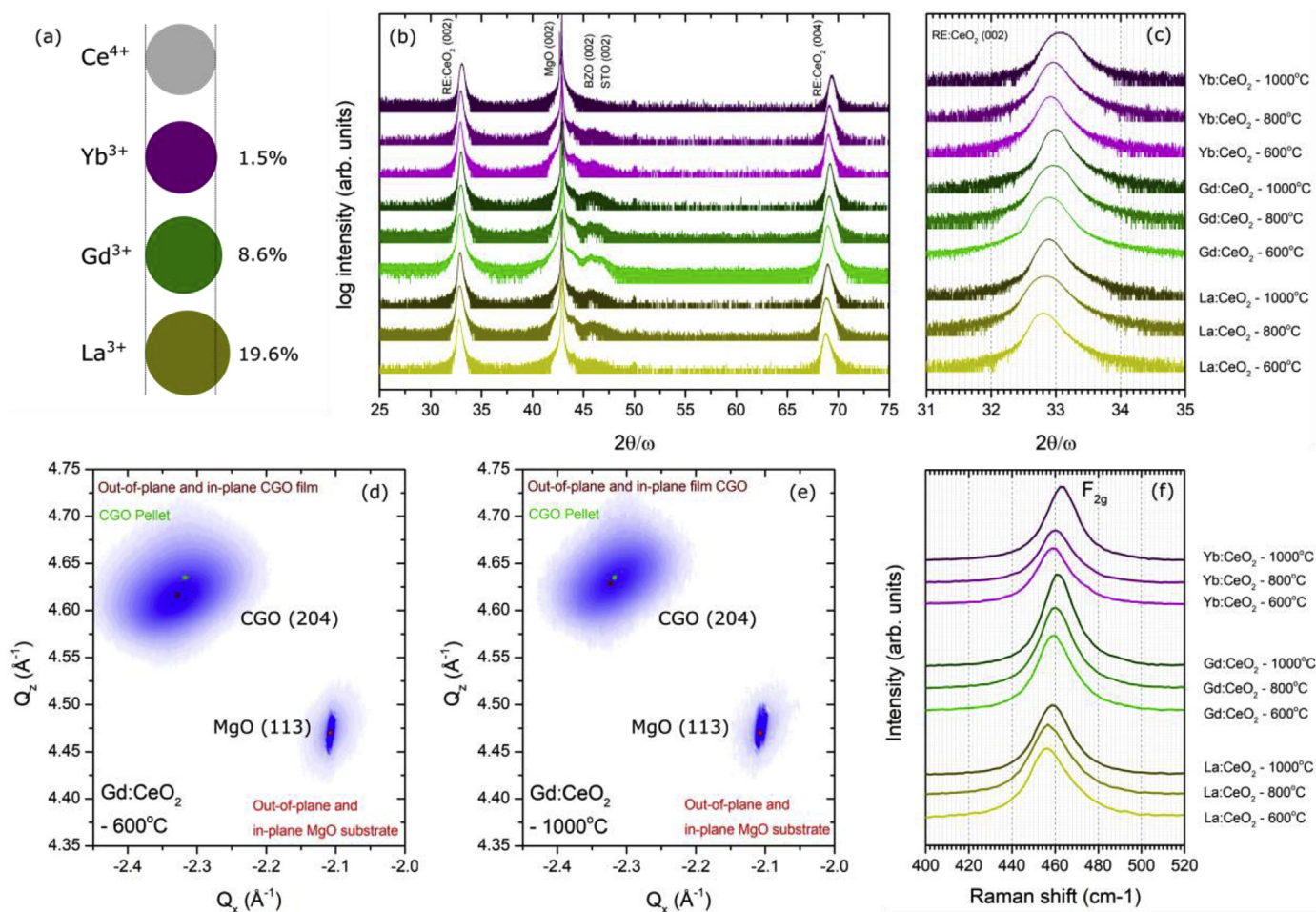


Fig. 1. (a) Ionic radii mismatch for the substitutional cations used. (b) Out-of-plane XRD $2\theta/\omega$ patterns for the films after annealing at different temperatures. (c) Detailed plot of the (002) RE:CeO₂ peak from the $2\theta/\omega$ patterns. (d,e) The RSMs of the Gd:CeO₂ films after annealing at (d) 600 °C and (e) 1000 °C. (f) Raman F_{2g} peak for the films after annealing at different temperatures.

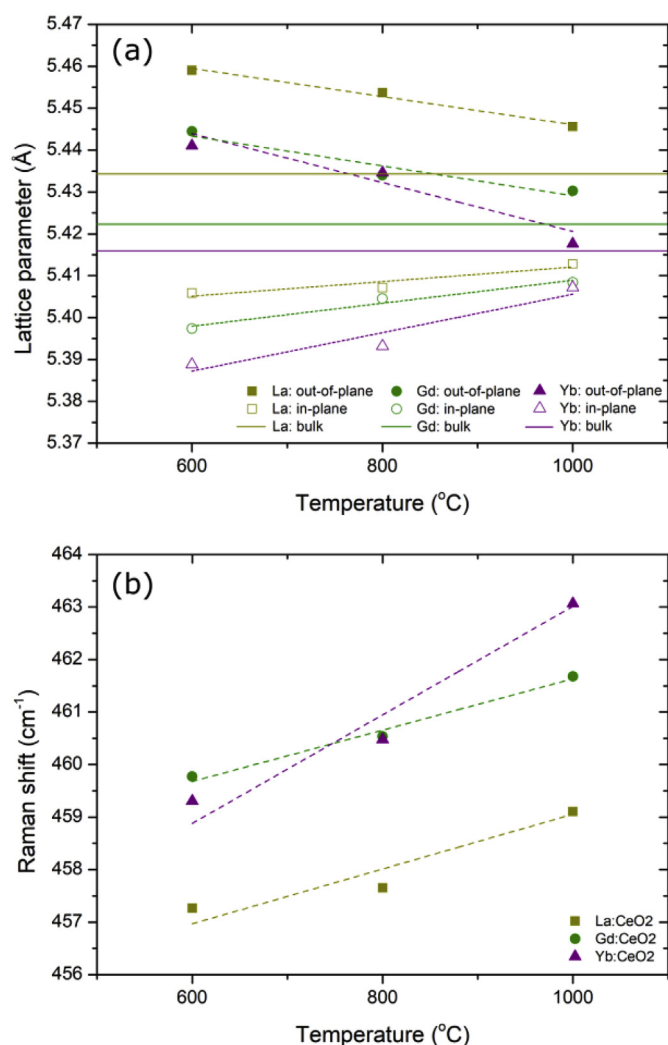


Fig. 2. (a) Out-of-plane (closed symbols) and in-plane (open symbols) lattice parameters as a function of annealing temperature. (b) F_{2g} peak Raman shift as a function of annealing temperature. The uncertainty on the data is smaller than the data markers.

and the Raman shifts plotted in Fig. 2b as a function of heat treatment temperature. Films annealed at 600 °C displayed a compressive in-plane strain of up to $\sim 0.5\%$ and a tensile out-of-plane strain of up to $\sim 0.45\%$, compared with lattice parameters extracted from the bulk pellets. The Raman shifts are in agreement with the out-of-plane lattice parameters. This is consistent with an in-plane compressive strain and out-of-plane Poisson relaxation, and represents a tetragonal distortion of the unit cell. As the temperature was increased, both sets of lattice parameters relaxed closer to the bulk values.

The origin of the lattice strain is not entirely clear. Comparing the lattice parameters of the STO buffer layer with RE:CeO₂ yields a lattice mismatch of between 1.6 and 1.9%, which would lead to tensile strain in the film and not explain the observed compressive in-plane strain. Also the thermal expansion coefficients between RE:CeO₂ and MgO at the growth temperature would not be sufficient to cause the observed strain [58,59], and the relatively large thickness of the films suggests that the strain is not localised at the interface. Both compressive and tensile stresses can occur for a variety of reasons during growth of physical vapour deposited films [60,61], and a systematic investigation of the growth processes was not the focus of this study. Regardless of the exact cause, the results

here show that the lattice strain could be systematically controlled via post growth annealing.

As discussed in Section 1, it is particularly important to ensure that grain boundaries are not playing a significant role in the conductivity of the films. Grain boundaries reduce the conductivity compared with single crystal bulk [62], can change the activation energy [51], relax interfacial lattice strain [63], and can have an inhomogeneous distribution in thin films [32,50]. Therefore transmission electron microscopy was used to study the microstructure of the films to ensure the films were of high quality and free from grain boundaries.

Fig. 3 shows representative TEM images taken on a Yb:CeO₂ film after annealing at 600 °C. A bright-field TEM image is shown in Fig. 3a, where the film can be seen to be dense and flat. The orientation relationship is confirmed from the selected area electron diffraction (SAED) pattern in the inset of Fig. 3a, and the high-angle annular dark field scanning TEM (HAADF-STEM) lattice image in Fig. 3b, where the registry is clearly maintained through the layers.

There is some contrast variation in Fig. 3a along the Yb:CeO₂ film that could be due to grain boundaries between columnar grains. In order to investigate this further HAADF-STEM was used to image the atomic structure at these regions. Fig. 3c shows a HAADF-STEM image of an area of the film where a clear change in contrast is seen, which could be interpreted as a grain boundary. The marked area was imaged at a higher magnification and shown in Fig. 3d, where the atomic structure is clearly visible. No sign of any tilting of the lattice plains, dislocations, or disorder is observed in these regions. This was the case for all regions imaged in the films. We, therefore, find no evidence for grain boundaries in the films in this study.

Dislocations could also be the cause of the observed changes in contrast. Although no edge dislocations running parallel to the beam direction were observed, threading dislocations through the films cannot be ruled out. A recent computational study on ionic transport in dislocations in trivalent cation substituted CeO₂ has shown that dislocations act to locally reduce oxygen ion diffusivity [64]. Therefore, given the small volume and one-dimensional nature of dislocations, they should have a negligible impact on the conductivity in the plane of the films.

The in-plane conductivity of the films and the grain core conductivity of the sintered pellets of the parent material are plotted over the full temperature range in Fig. 4. Typical Nyquist plots of the films and bulk material are shown in Fig. S3a and Fig. S4 in the Supplementary Information, respectively, along with the equivalent circuits used. The very good agreement between the conductivity of the films and the grain core conductivity of the pellets is strong evidence that the films are displaying oxygen ion conductivity, the films are free from grain boundaries, and that the buffer layers do not contribute to the conductance of the samples, as expected from previous studies [42,65].

A slight bending of the slopes can be seen for most films and pellets above 300 °C (shown more explicitly in Fig. S3b in the Supplementary Information), which has previously been reported for substituted CeO₂ and YSZ in the literature [3,8,66], and has been explained as the transition between a fully associated oxygen vacancy regime and a free vacancy regime. According to this interpretation, at low temperature, the activation energy is the sum of the migration and association enthalpies ($\Delta H_{\text{Mig.}} + \Delta H_{\text{Assoc.}}$) whereas at higher temperatures the activation energy is simply the migration enthalpy ($\Delta H_{\text{Mig.}}$). Recently Ahamer et al. have shown that the same bending can be fitted using a two barrier model, corresponding to a low energy barrier ($E_{a,1}$) dominating conductivity at low temperatures and a high energy barrier ($E_{a,2}$) dominating the high temperature behaviour [67]. The exact atomistic meaning of this model is not certain, and could be caused by either

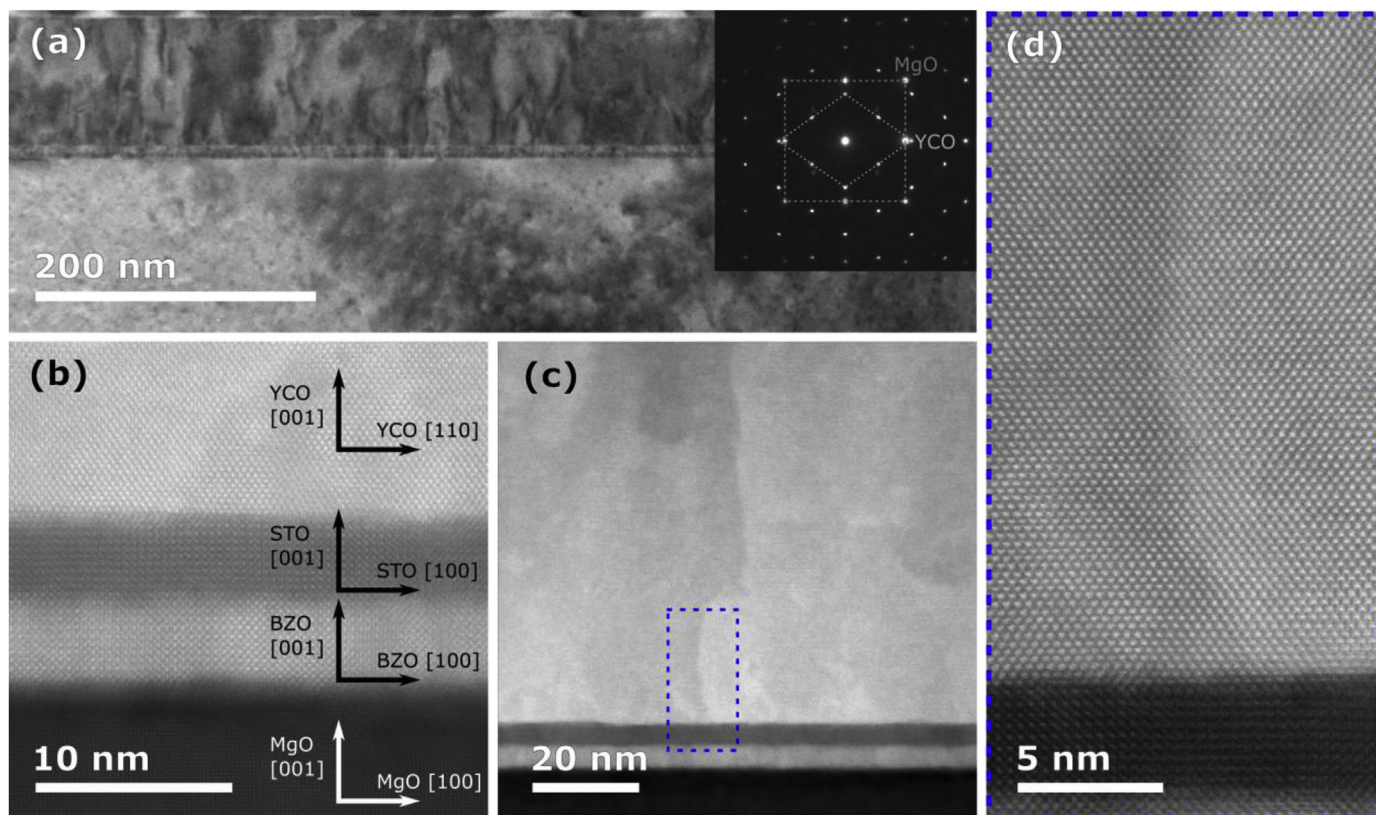


Fig. 3. Cross sectional TEM images taken of a Yb:CeO₂ film (YCO) after annealing at 600 °C and electrical testing. (a) Low magnification bright-field TEM micrograph with a SAED pattern in the inset. (b,c,d) High resolution HAADF-STEM images of the film. (d) is obtained from the dashed area in (c).

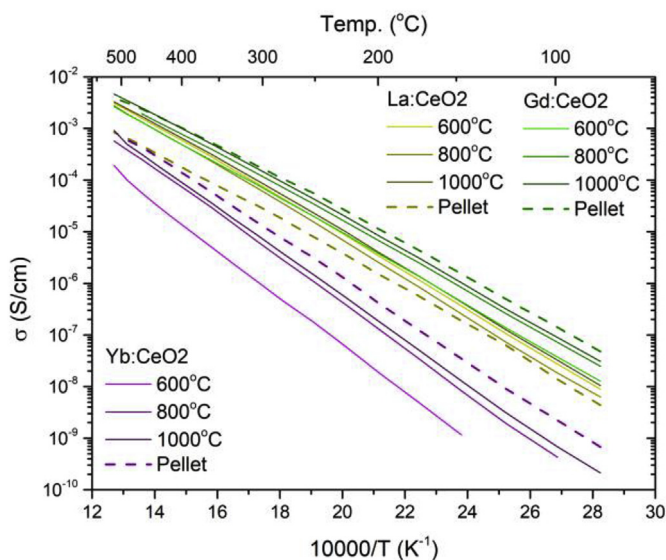


Fig. 4. Conductivity of all the films and the grain core from the pellets.

variations in the migration barrier height or deep trap states, due to the position of the substituted cations as well as the dynamic oxygen vacancy distribution.

Regardless, at low temperatures (<300 °C), where the conductivity obeys a linear Arrhenius relationship, the activation energy will be given by

$$E_a = \Delta H_{\text{Mig.}} + \Delta H_{\text{Assoc.}} \equiv E_{a,2} \quad [5]$$

depending on the model, but an effective activation energy which represents the complex energy landscape of varying migration barriers and site energies due to defect-defect interactions.

The conductivity of the films is plotted in Fig. 5a–c for each of the rare-earth substitutional cations in this low temperature “fully associated” regime. For the Gd and Yb cations, the conductivity is clearly reduced for the low temperature heat treatment at 600 °C, and displays an increase in activation energy. As the annealing temperature increases, and the strain is decreased, the conductivity approaches bulk values. The trend is not clear for La:CeO₂ which has a conductivity slightly above the bulk value, but still displays an increase in activation energy. The reason for this slight increase in conductivity above the bulk value is not clear at present.

Conceivably there are other reasons one might expect the conductivity to change after high temperature treatment. Grain growth would certainly lead to higher conductivity, but as shown by the TEM data, no evidence for grain boundaries was found in these films. Other effects such as cation ordering [12] or segregation to the surface [68] are also possible, but should result in a decrease in conductivity.

Fig. 6a shows the activation energy of the conductivity taken from the data in Fig. 5 and plotted as a function of in-plane lattice strain. A clear increase in activation barrier with in-plane compressive strain can be observed. The extracted pre-exponential factors shown in Fig. 6b show no systematic dependence on the strain present in the films, as expected. Interestingly, the activation energy of Yb:CeO₂ shows a much stronger

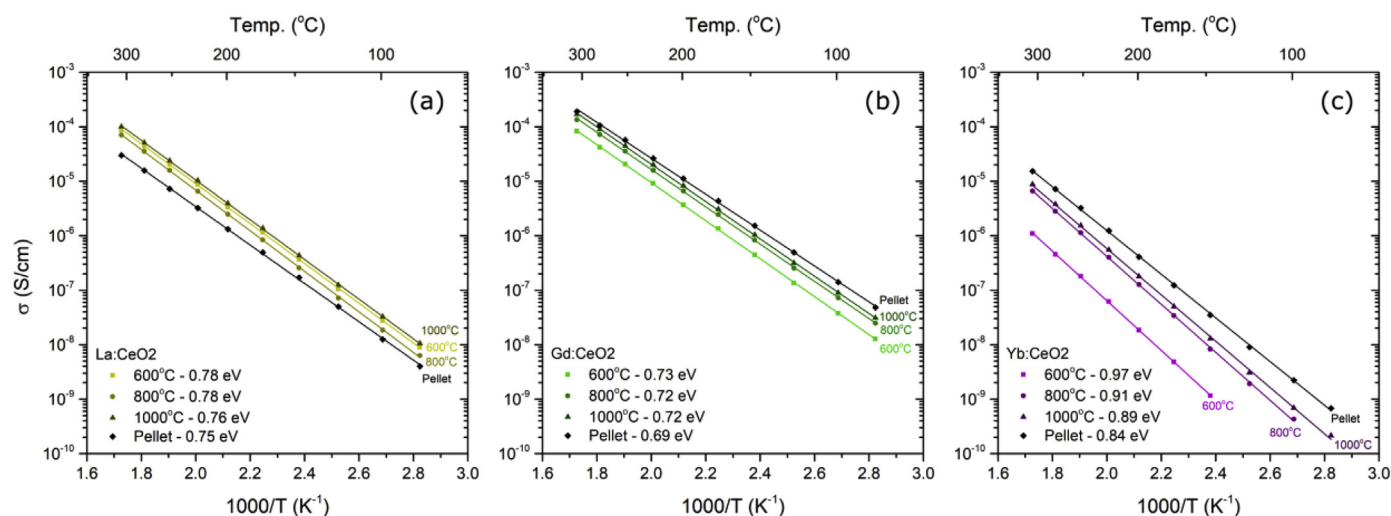


Fig. 5. Arrhenius plots of the conductivity for (a) La-, (b) Gd-, and (c) Yb-substituted CeO_2 films and bulk pellets for the low temperature ($<300^\circ\text{C}$) “fully associated” regime. The activation energies from the linear fits are displayed next to the data.

dependence on lattice strain than do Gd:CeO₂ or La:CeO₂. The possible reasons for this are discussed in detail later.

The observed increase in activation energy with compressive in-plane lattice strain is qualitatively in agreement with previous computational and experimental results on the effects of lattice strain on migration energy for oxygen vacancy hopping in fluorite materials as discussed in the introduction [13–26,63,69]. However, it is important to develop a quantitative consensus of strain effects, so that we can make predictions and more reliably attribute changes in ionic conductivity to lattice strain, when it is in fact the cause. This leads to the question: What is a practical and physically useful way to compare between literature results?

Korte et al. developed an elegant model to describe the effects of lattice strain in YSZ multilayer samples, which can be used for single films [63,69]. However, this model only applies to layers with a localised interfacial strain and conductivity measured as a function of layer thickness. The other challenges associated with comparisons with other studies are that the interfacial strain is often inferred from the lattice mismatch, which has since been shown not always to be the case for these systems [70]. Also the model is based on a conductivity or diffusivity value at an arbitrarily selected temperature, which could lead to significant differences if large changes in activation energy are observed.

Different changes in migration barrier with strain are expected

for different strain states (uniaxial, biaxial, hydrostatic) and for different hopping directions (in-plane or out-of-plane to the strained axes) [13,14]. Therefore it is essential that the same strain states and transport directions are compared. Here we opt to use the activation energy of the in-plane conductivity as a function of in-plane lattice strain, as it is both physically relevant and experimentally available. When comparing to other studies, it is crucial that a number of criteria are met to allow for a meaningful comparison. The strain must be axial, not localised to an interface, and the out-of-plane lattice parameter allowed to freely relax according to a Poisson dilation. The conductivity must be measured in-plane, along the biaxially strained direction, and not be affected by the presence of grain boundaries.

From the computational work on the effects of strain in CeO₂, some studies do not meet these criteria as they are based on hydrostatic [22,23], or uniaxial [21] strain, or do not report migration barriers parallel to the direction of the biaxial strain [71]. There are, however, four currently published studies that are suitable: two based on classical force field modelling on pure CeO₂ by De Souza et al. [13] and Y-substituted CeO₂ by Burbano et al. [19], and two from ab initio calculations on pure CeO₂ by Hinterberg et al. [14] and on Sm-substituted CeO₂ by Alaydrus et al. [20].

From experimental studies in the literature, Sanna et al. [72] and Mohan Kant et al. [37] displayed enhancements in conductivity over bulk behaviour, combined with anomalously high activation energies, that are not in agreement with strain modified migration barriers, and are deemed unsuitable for comparison. Hyodo et al. also attributed modified conductivity in Sm:CeO₂ laminated films to strain effects [38], but this has been shown not to be due to oxygen ion conductivity [73]. Qualitatively similar results, that is, increased activation energy with compressive strain or decreased activation energy with tensile strain, have been reported on Gd:CeO₂ films on Al₂O₃ by Rupp et al. [23], Gd:CeO₂/Er₂O₃ multilayers by Schweiger et al. [40], and Y:CeO₂/Ce_{1-x}Zr_xO₂ multilayers by Shen et al. [39], but none report the in-plane lattice parameters, nor the density of grain boundaries. A high density of grain boundaries can dominate the conductivity of physical vapour deposited thin films, often varying in density with film thickness [32,50], and have been shown to vary the activation energy as a function of grain size [51,74]. Lee et al. report strain-modified activation energy of epitaxial films of Gd:CeO₂ with minimal grain boundaries but did not assess the in-plane lattice parameters

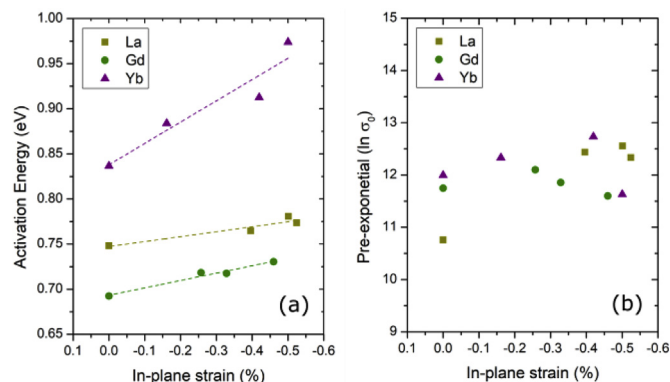


Fig. 6. The activation energies (a) and pre-exponential factors (b) taken from the low temperature, “fully associated” regime in Fig. 5.

[75]. Göbel et al. [50,76] observed no change in the activation energy of Gd:CeO₂ films when grown without grain boundaries. Yang et al. reported an enhancement in the conductivity of approximately one order-of-magnitude of Sm:CeO₂ over bulk behaviour when grown in the form of nanocomposite films [77]. However they did not observe any significant strain in the Sm:CeO₂ nanocomposite film, nor measured significant change in the activation energy. Recently, Ahn et al. also observed qualitatively similar results on Gd:CeO₂ films as a function of strain, but measured the conductivity out-of-plane, perpendicular to the biaxial strain direction [78], making a quantitative comparison with the work presented here of limited use.

A single experimental study satisfies the requirements for a suitable comparison. Fluri et al. showed a reduced activation energy as a function of tensile lattice strain for Sm:CeO₂ films grown on the same buffer layer system as used in this study. The in-plane strain was reported, the films were shown to have minimal grain boundaries, and the conductivity was close to the grain core value. The most significant difference is that all the strained samples exhibit tensile strain in the work by Fluri et al., while in our work, only compressive strain is studied.

Fig. 7 shows the activation energies of each of the suitable studies as a function of in-plane lattice strain. For all work, the strain is biaxial and the transport measured in-plane. For the computation works the lattice is strained along the [100] and [010] axes, and migration barriers are calculated along the [100] directions. The exception is that of Burbano et al., where the strain is along the (111) axes and average migration barriers in the [111] direction were calculated, which may lead to a different change in activation energy with strain [14]. For the experimental findings in this work and that by Fluri et al., the strain is biaxial in the [100] and [010] directions and the conductivity was measured in the [110] direction [42,79], which should be directly comparable to the computational studies describing films strained in the same direction.

The first thing to note about Fig. 7 is that all studies show that the activation energy increases with compressive strain and decreases with tensile strain, as expected. For the low strain values

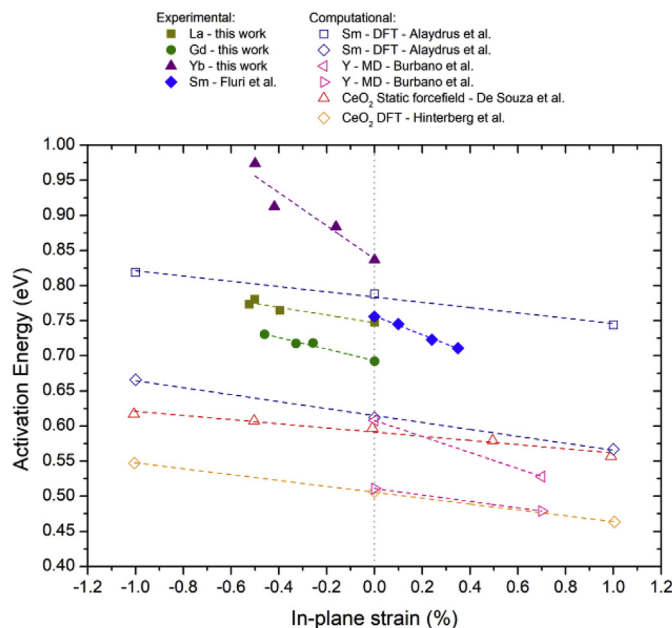


Fig. 7. Activation energy as a function of biaxial in-plane lattice strain for a range of experimental and computational studies. The details are given in Table 1.

plotted here ($\leq 1\%$), each study displays a linear change with lattice strain, although some of the computational work shows deviations from linear behaviour at larger strains ($>2\%$). All the studies are in reasonable agreement, with the slopes showing similar magnitudes in the change in activation energy with strain (-0.03 to -0.24 eV/%), showing for the first time a broad consensus amongst multiple experimental and computational studies on the effects of strain on the migration barrier in CeO₂.

From closer inspection of Fig. 7 it appears that the experimental work in this study and that of Fluri et al. show steeper slopes than those predicted by the majority of the computational studies. This could be due to effects in the experiments not captured in the simulations. Furthermore, from comparing just the data from the current work to avoid any variations due to the substitutional concentration or temperature range measured, a more substantial decrease in the activation energy with reduced compressive strain for Yb:CeO₂ is clearly observed than for Gd:CeO₂ or La:CeO₂. To investigate this, it is therefore useful to discuss the physical meaning of the gradients in Fig. 7.

The change in the activation energy with respect to pressure is given by [13,69]

$$\Delta V_a = \left(\frac{\partial E_a}{\partial p} \right)_T, \quad [6]$$

where ΔV_a is the activation volume. As a generalisation, the activation volume will be a tensor, which will describe the change in the activation energy for any stress states applied. However, for all the studies in Fig. 7, the stress and migration directions are equivalent and the activation volume can be treated as a scalar quantity. Therefore, for biaxial stress ($\sigma_{xx} = \sigma_{yy}$, $\sigma_{zz} = 0$), the effective pressure is

$$p_{\text{eff}} = -\frac{2}{3}\sigma_{xx}, \quad [7]$$

and the in-plane stress is given by

$$\sigma_{xx} = 3B \frac{1 - 2\nu}{1 - \nu} \varepsilon_{xx}, \quad [8]$$

where B is the bulk modulus and ν is the Poisson ratio, and ε_{xx} is the in-plane strain. One may then write Eq. (6) as

$$\frac{\partial E_a}{\partial \varepsilon_{xx}} = -2B \left(\frac{1 - 2\nu}{1 - \nu} \right) \Delta V_{\text{eff}} \quad [9]$$

Therefore, the slopes in Fig. 7 represent the effective activation volume of oxygen hopping in rare-earth substituted CeO₂ and may be expressed in units of $\text{cm}^3 \text{mol}^{-1}$. The slopes are given in Table 1. The values used for B and ν are taken from the literature and are 220 GPa and 0.33, respectively [80]. It should be noted that the values for ΔV_{eff} that we have calculated differ slightly from those originally calculated in the literature using the same data [13,14]. The reason for this is that we have fitted linear slopes to the data in Fig. 7 according to Eq. (9), rather than a higher order polynomial function over a much larger strain range. We have also used the same values for B and ν for each study, allowing us to fit all the data in Fig. 7 in a self-consistent manner which facilitates a more meaningful quantitative comparison. We will now consider why ΔV_{eff} would be larger for Yb:CeO₂ than Gd:CeO₂ or La:CeO₂.

As discussed above, there are two proposed models for describing defect-defect interactions in substituted fluorite materials: the defect associate model [66], and the two-barrier model [67]. If we first consider the defect associate model and assume the activation energy is a sum of migration enthalpy and associate

Table 1

Details of the studies and activation volumes for the data plotted in Fig. 7.

Reference	Type of study	M'_{ce}	Conc. (at. %)	ΔV_{eff} (cm ³ mol ⁻¹)	ΔV_{eff} (eV/% strain)
This work	Experimental – thin film	La	5	2.4	-0.055
This work	Experimental – thin film	Gd	5	3.5	-0.081
This work	Experimental – thin film	Yb	5	10.2	-0.236
Fluri et al. [42]	Experimental – thin film	Sm	15	5.7	-0.132
De Souza et al. [13]	Computational – Classical force field, static	None	–	1.3	-0.030
Burbano et al. [19]	Computational – Classical force field, MD	Y	8	4.9	-0.114
Burbano et al. [19]	Computational – Classical force field, MD	Y	12	2.0	-0.046
Hinterberg et al. [14]	Computational – DFT	None	–	1.8	-0.042
Alaydrus et al. [20]	Computational – DFT	Sm	Ce-Ce edge	2.1	-0.050
Alaydrus et al. [20]	Computational – DFT	Sm	Ce-Sm edge	1.6	-0.038

formation enthalpy ($\Delta H_{Mig.} + \Delta H_{Assoc.}$), then the effective activation volume can be split into the migration volume and the association volume, with each having straightforward physical meanings.

$$\Delta V_{eff} = \Delta V_{Mig.} + \Delta V_{Assoc.} \quad [10]$$

The migration volume is the expansion of the lattice as the oxygen ion resides in the saddle point between two vacant sites, and should be expansive for oxygen ion hopping in CeO₂. For the fluorite structured oxygen ion conductor YSZ, the migration volume has been measured as 2.08 cm³ mol⁻¹ [81], and for other fluorite structured anionic conductors, it is typically in the range of 2–4 cm³ mol⁻¹ (see Ref. [63] and references therein). The association volume is the difference in the volume of the lattice for associated defects and those at infinite distance.

$$\Delta V_{Assoc.} = \Delta V_{(v_o^{\cdot\cdot} + RE'_{ce})} - \Delta V_{(v_o^{\cdot\cdot})} - \Delta V_{(RE'_{ce})} \quad [11]$$

This could be either positive or negative, and may depend on the ionic radii of the cationic defect. Lubomirsky and co-workers have estimated an association volume as high as -9 cm³ mol⁻¹ for Gd-substituted CeO₂ [82,83], which is surprisingly large considering the relative size of the migration volume calculated for YSZ. However, the effect of substituent size on the migration volume is not known for CeO₂.

In this simplified model, the defect-defect interactions are described by the $\Delta H_{Assoc.}$ term which should be sensitive to the radii of the substitutional cations. Grieshammer et al. used ab initio modelling to calculate $\Delta H_{Assoc.}$ for rare-earth cations in CeO₂ [12]. They showed that the association energies for the oxygen vacancies and the rare-earth substituents in the nearest neighbour positions were -0.12 eV for La, -0.29 eV for Gd, and -0.48 eV for Yb, which follows the same trend as the calculated effective migration volumes in this study. However, they also demonstrated that for Yb, $\Delta H_{Assoc.}$ is very close to the Coulomb energy for pairs of charged particles separated by a distance a .

$$E_{Coulomb} = \frac{q_{v_o^{\cdot\cdot}} q_{RE'_{ce}}}{4\pi\epsilon_r\epsilon_0 a} \quad [12]$$

Where $q_{v_o^{\cdot\cdot}}$ and $q_{RE'_{ce}}$ are the effective charges of the oxygen vacancy and substituted cation respectively, ϵ_r is the relative dielectric constant of CeO₂ and ϵ_0 the dielectric constant of the vacuum. This is reasonable considering that the difference in the ionic radius of Yb³⁺ versus Ce⁴⁺ is only 1.5% in 8-fold coordination [84]. Clearly, if the Coulomb energy dominates the association enthalpy for Yb, then an approximately 0.5% change in the spacing of the ions in the lattice would lead to the same change for $\Delta H_{Assoc.}$, and would not explain the much larger sensitivity of Yb:CeO₂ to lattice strain than Gd:CeO₂ or La:CeO₂.

Alternatively, if we instead assume that the two barrier model suggested by Ahamer et al. [67] is a better physical representation

of the oxygen migration in substituted CeO₂, then the effective migration volume will be equal to the specific migration volume of the high energy barrier $E_{a,2}$.

$$\Delta V_{eff} = \Delta V_2 \quad [13]$$

Alaydrus et al. calculated the effect of strain on a number of different migration barriers in Sm substituted CeO₂ over edges with different Sm configurations. Two of these are plotted in Fig. 7,¹ but each displays nearly identical migration volumes.

There are no computational studies which provide an explanation for the difference in ΔV_{eff} for different substituent ionic radii that are directly and quantifiably comparable to the work presented here. However, Ahn et al. showed in DFT simulations of 18.75 mol.% Gd substituted CeO₂ that the energy barrier perpendicular to the biaxially strained direction was more sensitive to lattice strain for asymmetric substituent configurations than symmetric ones [71]. This describes whether the substituent configuration of the tetrahedron surrounding the oxygen ion at the start and end position of the jump are identical or not, suggesting that defect-defect interactions may affect the activation volume. Furthermore, in uniaxially strained CeO₂ investigated using molecular dynamics by Rushton et al. [21], it was shown that the activation energy for oxygen migration was more sensitive to strain for smaller substituents. In fact, calculating ΔV_{eff} from the published data ($\epsilon = 0 - 5\%$) yields a value of -0.034 eV/% for Yb, -0.028 eV/% for Gd, and -0.018 eV/% for La, which is qualitatively the same trend as observed in this work.

In order to investigate this further we carried out our own atomistic simulations. Using a classical force field simulation and the nudged elastic band method, the oxygen migration barriers are computed at 0.2 at.%, 5 at.% and 10 at.% substituent concentration with an in-plane biaxial strain of -5 to 1%. Unfortunately, values may not be directly comparable to our experimental studies since the classical force field simulation performed could not capture dielectric behaviour accurately. Furthermore, we find that the in-plane migration barriers show a minimal variation with strain, and instead the out-of-plane migration barriers are examined. Therefore, these simulations are only used for interpreting the qualitative trend observed experimentally, and are not plotted with our results for a quantitative comparison.

In the CeO₂ lattice, oxygen ion migrates over an edge containing two cations, which for rare-earth substituted CeO₂, may contain either none, one, or two substituted cations. Fig. 8 shows the calculated migration barriers over the Ce⁴⁺-Ce⁴⁺ edges and RE³⁺-Ce⁴⁺ edges for La, Gd and Yb substituted CeO₂ as a function of in-

¹ We have omitted the highest energy barrier corresponding to a jump past two substituted cations as it is much higher than anything experimentally reported (1.189 eV), and should represent a very small fraction of jump sites in RE_{0.05}Ce_{0.95}O_{2-δ}.

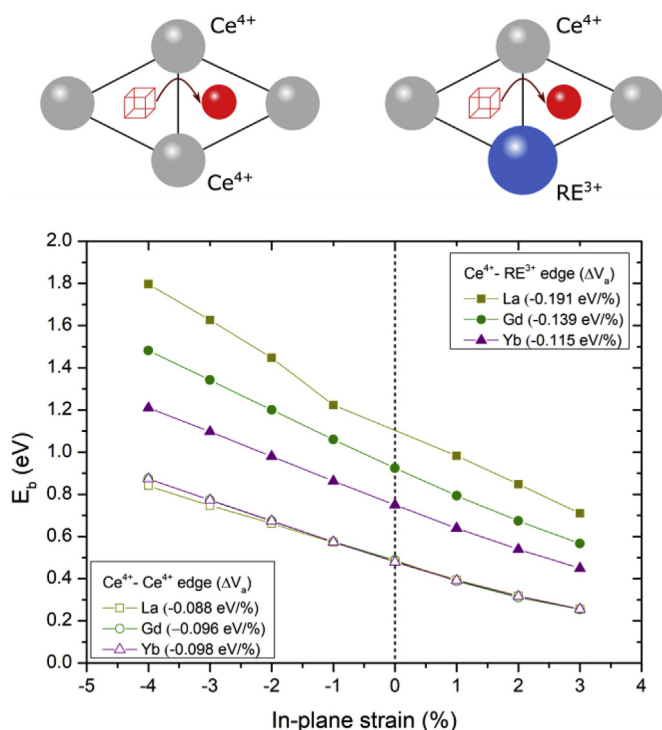


Fig. 8. The in-plane strain dependence of the oxygen migration barrier for the $\text{Ce}^{4+}-\text{Ce}^{4+}$ edge and the $\text{Ce}^{4+}-\text{RE}^{3+}$ edge, calculated from classical force field simulations. The uncertainty bars are smaller than the data symbols. The fitted activation volumes are given in the legend in units of eV/%. The edges are shown schematically above.

plane lattice strain. It was assumed that the migration barriers with two rare-earth cations would be both uncommon and have much higher migration barriers and therefore would not play a significant role in the transport properties. The activation volumes over each of the edges derived from the data in Fig. 8, are shown in the legend.

It can be seen that the migration barriers over $\text{RE}^{3+}-\text{Ce}^{4+}$ edges are more sensitive to strain and the size of substituent, compared with the ones over the $\text{Ce}^{4+}-\text{Ce}^{4+}$ edges. The migration barriers over the $\text{Ce}^{4+}-\text{Ce}^{4+}$ edges are always around 0.5 eV at zero strain regardless of the substituent species and the activation volumes are around 0.09–0.1 eV/%. In contrast, the migration barriers over $\text{RE}^{3+}-\text{Ce}^{4+}$ edge decreases as the size of the substituent decreases such that the $\text{Yb}^{3+}-\text{Ce}^{4+}$ edge has the lowest migration barrier among all three $\text{RE}^{3+}-\text{Ce}^{4+}$ edge cases. The activation volume for migration over the $\text{RE}^{3+}-\text{Ce}^{4+}$ edges behave similarly; it is the largest for the $\text{La}^{3+}-\text{Ce}^{4+}$ edge, second for the $\text{Gd}^{3+}-\text{Ce}^{4+}$ edge while the $\text{Yb}^{3+}-\text{Ce}^{4+}$ edge has the smallest activation volume, 0.1 eV/%, comparable to the activation volume over the $\text{Ce}^{4+}-\text{Ce}^{4+}$ edge. The trends are the same for the 5 at.%, and 10 at.% substituent concentrations and are shown in the Supplementary Information.

At first this may seem as a direct contradiction to the experimental results, but it should be noted that the barriers computed here are a “pure” migration barrier without any component of association energy. In fact, as shown in Table S3 and Table S4 in the Supplementary Information, the migration barriers in unstrained ceria and the activation volumes are very similar for all three defect concentrations. However, depending on the relative association between the vacancies and substituted cations, jumps over different edges will be more or less common for different substituents. Therefore, in order to interpret the experimental results, one needs to know the equilibrium distance between oxygen vacancy and the rare-earth cation.

Previous DFT simulations [12], classical force field simulations

[85] and XRD experiments [86] all show that the oxygen vacancies are more tightly bound to substituents in $\text{Yb}:\text{CeO}_2$, while less tightly bound in $\text{Gd}/\text{La}:\text{CeO}_2$. Based on these literature, it is reasonable to assume that a larger proportion of the jumps in $\text{Yb}:\text{CeO}_2$ take place over $\text{Yb}^{3+}-\text{Ce}^{4+}$ edge, while in $\text{Gd}/\text{La}:\text{CeO}_2$, the jumps over the $\text{Ce}^{4+}-\text{Ce}^{4+}$ edge are more prominent. Thus, the activation volume may be dominated by the strain dependence of the $\text{RE}^{3+}-\text{Ce}^{4+}$ edges for $\text{Yb}:\text{CeO}_2$, and the $\text{Ce}^{4+}-\text{Ce}^{4+}$ edges for $\text{Gd}/\text{La}:\text{CeO}_2$, resulting in the larger effective activation volume for Yb . However, providing a quantitative description of the interplay of these effects is left for future study.

Finally, in light of the results presented here, we will comment more broadly on the topic of strain modified transport in fluorite structured ionic conductors. Although here we have shown a moderate consistency between a number of computational and experimental studies, the slight changes in ΔV_{eff} reported will result in significant changes in conductivity at larger strains. For instance, if we assume the trend is the same for tensile and compressive strain, at 0.85% tensile strain the activation energy and the conductivity of the ‘non-optimised’ $\text{Yb}:\text{CeO}_2$ is the same as the ‘optimised’ $\text{Gd}:\text{CeO}_2$. Furthermore, recently Chueh and co-workers have fabricated coherent CeO_2 films on YSZ and STO substrates to strains as high as 5% [87,88]. If we were to assume the ΔV_{eff} values reported in this work were constant out to just 2% tensile strain, then this would yield a conductivity of $\sim 0.005 \text{ S cm}^{-1}$ for $\text{Gd}:\text{CeO}_2$ and $\sim 0.2 \text{ S cm}^{-1}$ for $\text{Yb}:\text{CeO}_2$ at 300 °C representing a 40 times higher conductivity for $\text{Yb}:\text{CeO}_2$ compared with $\text{Gd}:\text{CeO}_2$. Compared with bulk behaviour, this is more than a 10^4 increase over the bulk for $\text{Yb}:\text{CeO}_2$, in comparison to a ~ 27 fold increase for $\text{Gd}:\text{CeO}_2$.

Recently there has been growing interest in ionic transport in thin films at room temperature for memory applications such as oxide-based memristors [89–91]. Anionic-based switching devices require rapid ionic motion to occur in ambient conditions. Calculating the expected conductivity for 2% tensile strain at room temperature gives values of $\sim 3 \times 10^{-7} \text{ S cm}^{-1}$ for $\text{Gd}:\text{CeO}_2$ and $\sim 4 \times 10^{-4} \text{ S cm}^{-1}$ for $\text{Yb}:\text{CeO}_2$, such that the conductivity for $\text{Yb}:\text{CeO}_2$ is over 10^3 higher than $\text{Gd}:\text{CeO}_2$. Again, comparing to the bulk materials, this represents an enhancement of over 10^8 for $\text{Yb}:\text{CeO}_2$, compared to $10^{2.7}$ for $\text{Gd}:\text{CeO}_2$. Obviously, at this point these predictions are purely speculative, but they emphasize that the effects of the species and concentration of substitutional cations plays a particularly important role for strain modified conductivity that has, to date, mostly been overlooked. Here we demonstrate that much larger changes in the transport properties may be possible by selecting materials where there is a larger contribution of defect-defect interactions on the conductivity.

However, we must stress the importance of having a range of reasonable values of ΔV_{eff} which are in good agreement across a number of experimental and computations studies. For future studies on biaxially strained CeO_2 , changes in observed conductivity can be compared with these data to assess whether lattice strain is indeed the mechanism responsible. To facilitate ready comparison, we have also included ΔV_{eff} data in units of eV per percent strain in Table 1. If much larger variations in conductivity are observed than expected from the values of ΔV_{eff} presented here, then one should be cautious about attributing it to lattice strain.

4. Conclusions

We have grown epitaxial films of La, Gd, and Yb substituted CeO_2 by pulsed laser deposition, where the lattice strain has been systematically varied by thermal annealing. This has allowed the effect of strain on ionic conductivity to be examined without complications or ambiguity due to interfacial or grain boundary

effects. We find that for all substituents, the activation energy increases with increasing compressive biaxial strain. For ‘optimised’ materials, where the defect-defect interactions are minimised such as in Gd:CeO₂, the change in the activation energy with strain, characterised by the migration volume, are quantitatively comparable to previous computational and experimental findings. We stress the importance of building a numerical consensus in a field that has been plagued by inconsistency over the last decade.

For the ‘non-optimised’ material, Yb:CeO₂, we find that the activation energy is much more sensitive to lattice strain. For the same applied strain, the activation energy of Yb:CeO₂ was modified by approximately three times that of Gd:CeO₂. This demonstrates that there is a crucial interplay between strain and defect-defect interactions on ionic conductivity. We have rationalised our findings using force-field calculations that suggest that the cause may be due to a difference in barrier height change for different edge configurations, combined with a difference in jump distribution through the various edge configurations. This work implies that substantially larger changes in transport properties can be obtained for ‘non-optimised’ electrolyte materials compared to ‘optimised’ electrolyte materials and can be understood through consideration of defect association.

Acknowledgements

GFH thanks R. De Souza and J. Kilner for illuminating discussions, and J. Santiso for assistance with the XRD RSM analysis. GFH also gratefully acknowledges financial support from a Kakenhi Grant-in-Aid for Encouragement of Young Scientists (B) Award (No. JP16K18235). The authors are also grateful for support from the Progress 100 program of Kyushu University, and the International Institute for Carbon-Neutral Energy Research (WPI-I2CNER), both supported by MEXT, Japan, and the Center of Innovation Science and Technology based Radical Innovation and Entrepreneurship Program (COI Program), by the Japan Science and Technology Agency (JST). L. Sun, B. Yildiz and H. L. Tuller acknowledge support for their research from the Department of Energy, Basic Energy Sciences under award number DE-SC0002633 (Chemomechanics of Far-From-Equilibrium Interfaces).

Appendix A. Supplementary data

Supplementary data to this article can be found online at <https://doi.org/10.1016/j.actamat.2018.12.058>.

References

- [1] C.A.J. Fisher, V.M. Hart Prieto, M.S. Islam, Lithium battery materials LiMPO₄ (M = Mn, Fe, Co, and Ni): insights into defect association, transport mechanisms, and doping behavior, *Chem. Mater.* 20 (2008) 5907–5915.
- [2] M. Saiful Islam, Ionic transport in ABO₃ perovskite oxides: a computer modelling tour, *J. Mater. Chem.* 10 (2000) 1027–1038.
- [3] D. Wang, D. Park, J. Griffith, A. Nowick, Oxygen-ion conductivity and defect interactions in yttria-doped ceria, *Solid State Ionics* 2 (1981) 95–105.
- [4] J. Kilner, R. Brook, A study of oxygen ion conductivity in doped non-stoichiometric oxides, *Solid State Ionics* 6 (1982) 237–252.
- [5] T. Mori, J. Drennan, J.H. Lee, J.G. Li, T. Ikegami, Oxide ionic conductivity and microstructures of Sm- or La-doped CeO₂-based systems, *Solid State Ionics* 154–155 (2002) 461–466.
- [6] T. Mori, J. Drennan, Y. Wang, J.-H. Lee, J.-G. Li, T. Ikegami, Electrolytic properties and nanostructural features in the La₂O₃-CeO₂ system, *J. Electrochem. Soc.* 150 (2003) A665–A673.
- [7] T.S. Zhang, J. Ma, L.B. Kong, S.H. Chan, J.A. Kilner, Aging behavior and ionic conductivity of ceria-based ceramics: a comparative study, *Solid State Ionics* 170 (2004) 209–217.
- [8] J. Faber, C. Geoffroy, A. Roux, A. Sylvestre, P. Abélard, A Systematic investigation of the dc electrical conductivity of rare-earth doped ceria, *Appl. Phys. A* 49 (1989) 225–232.
- [9] M. Mogensen, N.M. Sammes, G.A. Tompsett, Physical, chemical and electrochemical properties of pure and doped ceria, *Solid State Ionics* 129 (2000) 63–94.
- [10] J.A. Kilner, Fast oxygen transport in acceptor doped oxides, *Solid State Ionics* 129 (2000) 13–23.
- [11] D. Marrocchelli, S.R. Bishop, H.L. Tuller, B. Yildiz, Understanding chemical expansion in non-stoichiometric oxides: ceria and zirconia case studies, *Adv. Funct. Mater.* 22 (2012) 1958–1965.
- [12] S. Grieshammer, B.O.H. Grope, J. Koettgen, M. Martin, A combined DFT + U and Monte Carlo study on rare earth doped ceria, *Phys. Chem. Chem. Phys.* 16 (2014) 9974–9986.
- [13] R.A. De Souza, A. Ramadan, S. Hörner, Modifying the barriers for oxygen-vacancy migration in fluorite-structured CeO₂ electrolytes through strain: a computer simulation study, *Energy Environ. Sci.* 5 (2012) 5445–5453.
- [14] J. Hinterberg, T. Zacherle, R. A. De Souza, Activation volume tensor for oxygen-vacancy migration in strained CeO₂ electrolytes, *Phys. Rev. Lett.* 110 (2013).
- [15] A. Kushima, B. Yildiz, Oxygen ion diffusivity in strained yttria stabilized zirconia: where is the fastest strain? *J. Mater. Chem.* 20 (2010) 4809–4819.
- [16] D.S. Aidhy, B. Liu, Y. Zhang, W.J. Weber, Strain-induced phase and oxygen-vacancy stability in ionic interfaces from first-principles calculations, *J. Phys. Chem. C* 118 (2014) 30139–30144.
- [17] M. Oka, H. Kamisaka, T. Fukumura, T. Hasegawa, DFT-based ab initio MD simulation of the ionic conduction in doped ZrO₂ systems under epitaxial strain, *Phys. Chem. Chem. Phys.* 17 (2015) 29057–29063.
- [18] A. Tarancón, A. Morata, New insights into the origin of the oxide ionic diffusion change in strained lattices of yttria stabilized zirconia, *Comput. Mater. Sci.* 103 (2015) 206–215.
- [19] M. Burbano, D. Marrocchelli, G.W. Watson, Strain effects on the ionic conductivity of Y-doped ceria: a simulation study, *J. Electroceram.* 32 (2013) 28–36.
- [20] M. Alaydrus, M. Sakaue, S.M. Aspera, T.D.K. Wungu, N.H. Linh, T.P.T. Linh, H. Kasai, T. Ishihara, T. Mohri, A DFT+U study of strain-dependent ionic migration in Sm-Doped Ceria, *J. Phys. Soc. Japan.* 83 (2014).
- [21] M.J.D. Rushton, A. Chronos, Impact of uniaxial strain and doping on oxygen diffusion in CeO₂, *Sci. Rep.* 4 (2014) 6048.
- [22] M.J.D. Rushton, A. Chronos, S.J. Skinner, J.A. Kilner, R.W. Grimes, Effect of strain on the oxygen diffusion in yttria and gadolinia co-doped ceria, *Solid State Ionics* 230 (2013) 37–42.
- [23] J.L.M. Rupp, E. Fabbri, D. Marrocchelli, J.W. Han, D. Chen, E. Traversa, H.L. Tuller, B. Yildiz, Scalable oxygen-ion transport kinetics in metal-oxide films: impact of thermally induced lattice compaction in acceptor doped ceria films, *Adv. Funct. Mater.* 24 (2014) 1562–1574.
- [24] W. Araki, Y. Imai, T. Adachi, Mechanical stress effect on oxygen ion mobility in 8 mol% yttria-stabilized zirconia electrolyte, *J. Eur. Ceram. Soc.* 29 (2009) 2275–2279.
- [25] F. Li, R. Lu, H. Wu, E. Kan, C. Xiao, K. Deng, D.E. Ellis, The strain effect on colossal oxygen ionic conductivity in nanoscale zirconia electrolytes: a first-principles-based study, *Phys. Chem. Chem. Phys.* 15 (2013) 2692–2697.
- [26] W. Araki, Y. Arai, Oxygen diffusion in yttria-stabilized zirconia subjected to uniaxial stress, *Solid State Ionics* 181 (2010) 441–446.
- [27] S. Sanna, V. Esposito, D. Pergolesi, A. Orsini, A. Tebano, S. Licoccia, G. Balestrino, E. Traversa, Fabrication and electrochemical properties of epitaxial samarium-doped ceria films on SrTiO₃-buffered MgO substrates, *Adv. Funct. Mater.* 19 (2009) 1713–1719.
- [28] A. Karthikeyan, C.L. Chang, S. Ramanathan, High temperature conductivity studies on nanoscale yttria-doped zirconia thin films and size effects, *Appl. Phys. Lett.* 89 (2006) 183116.
- [29] M. Sillarsen, P. Eklund, N. Pryds, E. Johnson, U. Helmersson, J. Böttiger, Low-temperature superionic conductivity in strained yttria-stabilized zirconia, *Adv. Funct. Mater.* 20 (2010) 2071–2076.
- [30] M. Gerstl, G. Friedbacher, F. Kubel, H. Hutter, J. Fleig, The relevance of interfaces for oxide ion transport in yttria stabilized zirconia (YSZ) thin films, *Phys. Chem. Chem. Phys.* 15 (2013) 1097–1107.
- [31] J. Jiang, X. Hu, W. Shen, C. Ni, J.L. Hertz, Improved ionic conductivity in strained yttria-stabilized zirconia thin films, *Appl. Phys. Lett.* 102 (2013) 143901.
- [32] G.F. Harrington, A. Cavallaro, D.W. McComb, S.J. Skinner, J.A. Kilner, The effects of lattice strain, dislocations, and microstructure on the transport properties of YSZ films, *Phys. Chem. Chem. Phys.* 19 (2017) 14319–14336.
- [33] C. Korte, A. Peters, J. Janek, D. Hesse, N. Zakharov, Ionic conductivity and activation energy for oxygen ion transport in superlattices-the semicoherent multilayer system YSZ (ZrO₂ + 9.5 mol% Y₂O₃)/Y₂O₃, *Phys. Chem. Chem. Phys.* 10 (2008) 4623–4635.
- [34] N. Schichtel, C. Korte, D. Hesse, N. Zakharov, B. Butz, D. Gerthsen, J. Janek, On the influence of strain on ion transport: microstructure and ionic conductivity of nanoscale YSZ/Sc₂O₃ multilayers, *Phys. Chem. Chem. Phys.* 12 (2010) 14596–14608.
- [35] D. Pergolesi, E. Fabbri, S.N. Cook, V. Roddatis, E. Traversa, J. A. Kilner, Tensile lattice distortion does not affect oxygen transport in yttria-stabilized zirconia-CeO₂ heterointerfaces, *ACS Nano* 6 (2012) 10524–10534.
- [36] B. Li, J. Zhang, T. Kaspar, V. Shutthanandan, R.C. Ewing, J. Lian, Multilayered YSZ/GZO films with greatly enhanced ionic conduction for low temperature solid oxide fuel cells, *Phys. Chem. Chem. Phys.* 15 (2013) 1296–1301.
- [37] K. Mohan Kant, V. Esposito, N. Pryds, Strain induced ionic conductivity enhancement in epitaxial Ce_{0.9}Gd_{0.1}O_{2-δ} thin films, *Appl. Phys. Lett.* 100 (2012) 033105.
- [38] J. Hyodo, S. Ida, J.A. Kilner, T. Ishihara, Electronic and oxide ion conductivity in

- Pr₂Ni_{0.71}Cu_{0.24}Ga_{0.05}O₄/Ce_{0.8}Sm_{0.2}O₂ laminated film, *Solid State Ionics* 230 (2013) 16–20.
- [39] W. Shen, J. Jiang, J.L. Hertz, Reduced ionic conductivity in biaxially compressed ceria, *RSC Adv.* 4 (2014) 21625–21630.
- [40] S. Schweiger, M. Kubicek, F. Messerschmitt, C. Murer, J.L.M. Rupp, A microdot multilayer oxide device: let us tune the strain-ionic transport interaction, *ACS Nano* 8 (2014) 5032–5048.
- [41] Y. Shi, A.H. Bork, S. Schweiger, J.L.M. Rupp, The effect of mechanical twisting on oxygen ionic transport in solid-state energy conversion membranes, *Nat. Mater.* 14 (2015) 721–727.
- [42] A. Fluri, D. Pergolesi, V. Roddatis, A. Wokaun, T. Lippert, In situ stress observation in oxide films and how tensile stress influences oxygen ion conduction, *Nat. Commun.* 7 (2016) 10692.
- [43] X. Guo, E. Vasco, S. Mi, K. Szot, E. Wachsman, R. Waser, Ionic conduction in zirconia films of nanometer thickness, *Acta Mater.* 53 (2005) 5161–5166.
- [44] I. Kosacki, C.M. Rouleau, P.F. Becher, J. Bentley, D.H. Lowndes, Nanoscale effects on the ionic conductivity in highly textured YSZ thin films, *Solid State Ionics* 176 (2005) 1319–1326.
- [45] B. Yildiz, “Stretching” the energy landscape of oxides—effects on electrocatalysis and diffusion, *MRS Bull.* 39 (2014) 147–156.
- [46] K. Wen, W. Lv, W. He, Interfacial lattice-strain effects on improving the overall performance of micro-solid oxide fuel cells, *J. Mater. Chem. A* 3 (2015) 20031–20050.
- [47] N.H. Perry, G.F. Harrington, H.L. Tuller, Electrochemical ionic interfaces, in: N. Pryds, V. Esposito, G. Korotcenkov (Eds.), *Met. Oxide-Based Thin Film Struct.*, Elsevier Inc, 2018, pp. 79–106.
- [48] H.-R. Kim, J.-C. Kim, K.-R. Lee, H.-I. Ji, H.-W. Lee, J.-H. Lee, J.-W. Son, “Illusional” nano-size effect due to artifacts of in-plane conductivity measurements of ultra-thin films, *Phys. Chem. Chem. Phys.* 13 (2011) 6133–6137.
- [49] H.J. Avila-Paredes, J. Zhao, S. Wang, M. Pietrowski, R.A. De Souza, A. Reinholdt, Z.A. Munir, M. Martin, S. Kim, Protonic conductivity of nano-structured yttria-stabilized zirconia: dependence on grain size, *J. Mater. Chem.* 20 (2010) 990–994.
- [50] M.C. Göbel, G. Gregori, X. Guo, J. Maier, Boundary effects on the electrical conductivity of pure and doped cerium oxide thin films, *Phys. Chem. Chem. Phys.* 12 (2010) 14351–14361.
- [51] T.C. Yeh, N.H. Perry, T.O. Mason, Nanograin composite model studies of nanocrystalline gadolinia-doped ceria, *J. Am. Ceram. Soc.* 94 (2011) 1073–1078.
- [52] J. Keppner, J. Schubert, M. Ziegner, B. Mogwitz, J. Janek, C. Korte, Influence of texture and grain misorientation on the ionic conduction in multilayered solid electrolytes – interface strain effects in competition with blocking grain boundaries, *Phys. Chem. Chem. Phys.* 20 (2018) 9269–9280.
- [53] M. Gerstl, E. Navickas, G. Friedbacher, F. Kubel, M. Ahrens, J. Fleig, The separation of grain and grain boundary impedance in thin yttria stabilized zirconia (YSZ) layers, *Solid State Ionics* 185 (2011) 32–41.
- [54] R.A. De Souza, V. Metlenko, D. Park, T.E. Weirich, Behavior of oxygen vacancies in single-crystal SrTiO₃: equilibrium distribution and diffusion kinetics, *Phys. Rev. B* 85 (2012) 174109.
- [55] S. Plimpton, Fast parallel algorithms for short-range molecular dynamics, *J. Comput. Phys.* 117 (1995) 1–19.
- [56] L. Minervini, M.O. Zacate, R.W. Grimes, Defect cluster formation in M₂O₃-doped CeO₂, *Solid State Ionics* 116 (1999) 339–349.
- [57] W.H. Weber, K.C. Hass, J.R. McBride, Raman study of CeO₂: second-order scattering, lattice dynamics and particle-size effects, *Phys. Rev. B* 48 (1993) 178–185.
- [58] H. Hayashi, Thermal expansion of Gd-doped ceria and reduced ceria, *Solid State Ionics* 132 (2000) 227–233.
- [59] G.K. White, L. Anderson, Gruneisen parameter of magnesium oxide, *J. Appl. Phys.* 37 (1966) 430–432.
- [60] E. Chason, A kinetic analysis of residual stress evolution in polycrystalline thin films, *Thin Solid Films* 526 (2012) 1–14.
- [61] E. Chason, P.R. Guduru, Tutorial: understanding residual stress in polycrystalline thin films through real-time measurements and physical models, *J. Appl. Phys.* 119 (2016) 191101.
- [62] X. Guo, R. Waser, Electrical properties of the grain boundaries of oxygen ion conductors: acceptor-doped zirconia and ceria, *Prog. Mater. Sci.* 51 (2006) 151–210.
- [63] C. Korte, J. Keppner, A. Peters, N. Schichtel, H. Aydin, J. Janek, Coherency strain and its effect on ionic conductivity and diffusion in solid electrolytes – an improved model for nanocrystalline thin films and a review of experimental data, *Phys. Chem. Chem. Phys.* 16 (2014) 24575–24591.
- [64] L. Sun, D. Marrocchelli, B. Yildiz, Edge dislocation slows down oxide ion diffusion in doped CeO₂ by segregation of charged defects, *Nat. Commun.* 6 (2015) 6294.
- [65] D. Pergolesi, V. Roddatis, E. Fabbri, C.W. Schneider, T. Lippert, E. Traversa, J.A. Kilner, Probing the bulk ionic conductivity by thin film hetero-epitaxial engineering, *Sci. Technol. Adv. Mater.* 16 (2015) 015001.
- [66] P.S. Manning, J.D. Sirman, R.A. De Souza, J.A. Kilner, The kinetics of oxygen transport in 9.5 mol % single crystal yttria stabilised zirconia, *Solid State Ionics* 100 (1997) 1–10.
- [67] C. Ahamer, A.K. Opitz, G.M. Rupp, J. Fleig, Revisiting the temperature dependent ionic conductivity of yttria stabilized zirconia (YSZ), *J. Electrochem. Soc.* 164 (2017) F790–F803.
- [68] G.F. Harrington, S.J. Skinner, J.A. Kilner, Can solute segregation in ceramic materials be reduced by lattice strain? *J. Am. Ceram. Soc.* 101 (2018) 1310–1322.
- [69] C. Korte, N. Schichtel, D. Hesse, J. Janek, Influence of interface structure on mass transport in phase boundaries between different ionic materials: experimental studies and formal considerations, *Monatshefte Fur Chemie* 140 (2009) 1069–1080.
- [70] J. Keppner, C. Korte, J. Schubert, W. Zander, M. Ziegner, D. Stolten, XRD analysis of strain states in epitaxial YSZ/RE₂O₃ (RE = Y, Er) multilayers as a function of layer thickness, *Solid State Ionics* 273 (2015) 2–7.
- [71] J. Ahn, S. Choi, K.J. Yoon, J.W. Son, B.K. Kim, J.H. Lee, H.W. Jang, H. Kim, Strain-Induced tailoring of oxygen-ion transport in highly doped CeO₂ electrolyte: effects of biaxial extrinsic and local lattice strain, *ACS Appl. Mater. Interfaces* 9 (2017) 42415–42419.
- [72] S. Sanna, V. Esposito, A. Tebano, S. Licocchia, E. Traversa, G. Balestrino, Enhancement of ionic conductivity in sm-doped ceria/yttria-stabilized zirconia heteroepitaxial structures, *Small* 6 (2010) 1863–1867.
- [73] S.N. Cook, PhD Thesis, Imperial College London, 2012.
- [74] J.L.M. Rupp, Ionic diffusion as a matter of lattice-strain for electroceramic thin films, *Solid State Ionics* 207 (2012) 1–13.
- [75] K.R. Lee, K. Ahn, Y.C. Chung, J.H. Lee, H.I. Yoo, Lattice distortion effect on electrical properties of GDC thin films: experimental evidence and computational simulation, *Solid State Ionics* 229 (2012) 45–53.
- [76] M.C. Göbel, G. Gregori, J. Maier, Size effects on the electrical conductivity of ceria: achieving low space charge potentials in nanocrystalline thin films, *J. Phys. Chem. C* 117 (2013) 22560–22568.
- [77] S.M. Yang, S. Lee, J. Jian, W. Zhang, P. Lu, Q. Jia, H. Wang, T. Won Noh, S.V. Kalinin, J.L. MacManus-Driscoll, Strongly enhanced oxygen ion transport through samarium-doped CeO₂ nanopillars in nanocomposite films, *Nat. Commun.* 6 (2015) 8588.
- [78] J. Ahn, H.W. Jang, H.-I. Ji, H. Kim, K.J. Yoon, J.-W. Son, B.-K. Kim, H.-W. Lee, J.-H. Lee, Identification of actual strain-induced effect on fast ion conduction in thin film electrolyte, *Nano Lett.* 18 (2018) 2794–2801.
- [79] A. Fluri, Personal Communication, 2017.
- [80] A. Selçuk, A. Atkinson, Elastic properties of ceramic oxides used in solid oxide fuel cells (SOFC), *J. Eur. Ceram. Soc.* 17 (1997) 1523–1532.
- [81] E.T. Park, J.-H. Park, Pressure effect on ionic conductivity in yttrium-oxide-doped single crystal-zirconium oxide, in: 3rd Int. Meet. Pacific Rim Ceram. Soc. Kyungju, Korea, 1998.
- [82] M. Greenberg, E. Wachtel, I. Lubomirsky, J. Fleig, J. Maier, Elasticity of solids with a large concentration of point defects, *Adv. Funct. Mater.* 16 (2006) 48–52.
- [83] A. Kossov, Y. Feldman, E. Wachtel, I. Lubomirsky, J. Maier, Elasticity of solids with a large concentration of point defects II. The chemical strain effect in Ce_{0.8}Gd_{0.2}O_{1.9}, *Adv. Funct. Mater.* 17 (2007) 2393–2398.
- [84] R.D. Shannon, C.T. Prewitt, Effective ionic radii in oxides and fluorides, *Acta Crystallogr.* 25 (1969) 925–946.
- [85] M. Burbano, S. Nadin, D. Marrocchelli, M. Salanne, G.W. Watson, Ceria co-doping: synergistic or average effect? *Phys. Chem. Chem. Phys.* 16 (2014) 8320–8331.
- [86] A. Nakamura, New defect-crystal-chemical approach to non-Vegardianity and complex defect structure of fluorite-based MO₂-LnO_{1.5} solid solutions (M⁴⁺ = Ce, Th; Ln³⁺ = lanthanide): Part II: Detailed local-structure and ionic-con, *Solid State Ionics* 181 (2010) 1631–1653.
- [87] Y. Shi, S.C. Lee, M. Monti, C. Wang, Z.A. Feng, W.D. Nix, M.F. Toney, R. Sinclair, W.C. Chueh, Growth of highly strained CeO₂ ultrathin films, *ACS Nano* 16 (2016) 9938–9947.
- [88] C. Balaji Gopal, M. García-Melchor, S.C. Lee, Y. Shi, A. Shavorskiy, M. Monti, Z. Guan, R. Sinclair, H. Bluhm, A. Vojvodic, W.C. Chueh, Equilibrium oxygen storage capacity of ultrathin CeO_{2-δ} depends non-monotonically on large biaxial strain, *Nat. Commun.* 8 (2017) 15360.
- [89] R. Waser, M. Aono, Nanoionics-based resistive switching memories, *Nat. Mater.* 6 (2007) 833–840.
- [90] R. Waser, R. Dittmann, C. Staikov, K. Szot, Redox-based resistive switching memories nanoionic mechanisms, prospects, and challenges, *Adv. Mater.* 21 (2009) 2632–2663.
- [91] J.J. Yang, D.B. Strukov, D.R. Stewart, Memristive devices for computing, *Nat. Nanotechnol.* 8 (2013) 13–24.